A Ga-Sn Liquid Metal Mediated Structural Cathode for Li-O_2 Batteries

Zhihong Luo[2], Chenhao Ji[2], Liankun Yin[2], Guangbin Zhu[2], Ben Bin Xu[3], Yucheng Wang[3], Terence Xiaoteng Liu[3*], Xiangqun Zhuge[1], Kun Luo[1*]

1. School of Materials Science and Engineering, Changzhou University, Changzhou 213164, P R China;

2. College of Materials Science and Engineering, Guilin University of Technology, Guilin 541004, P R China;

3. Department of Mechanical & Construction Engineering, Faculty of Engineering and Environment, Northumbria University, Newcastle upon Tyne, NE1 8ST, UK.

KEYWORDS: Li-O_2 batteries, Ga-Sn liquid metal, flaky Li_2O_2, cathode passivation

ABSTRACT: One of the recent challenges in Li-O_2 battery technology is the cycle life, which can be severely shortened by cathode passivation induced by discharge product accumulation; this can be eliminated by reducing the amount of discharge products. Herein, we report a feasibility study on the development of a Ga-Sn liquid metal (LM) functionalized multi-walled carbon nanotubes (MWNTs) cathode. In a comparison of MWNT, LM, m-LM/MWNT (pre-mixed LM and MWNTs), and LM/MWNT (LM modified MWNTs) cathodes, morphology analysis showed that small Li_2O_2 flakes rather than large crystals grown on the conductive Ga-Sn LM and MWNTs of the LM/MWNT

cathode only. The decomposition of the flaky Li_2O_2 on the LM/MWNT cathode occurred at lower charge overpotentials, resulting in low polarization; thus, the cathode passivation and the consumption of the Li anode were both alleviated during the cyclic process. The LM/MWNT cathode significantly improved the cycle life, rate performance and ultimate capacity of Li-O_2 batteries.

INTRODUCTION

Aprotic Li-O_2 batteries (LOBs) are well known for their high theoretical specific energy density (11400 Wh kg^{-1}), [1-2] which is significantly higher than those of Zn-air, aluminium ions, sodium ion and popular lithium-ion batteries. [3-6] However, challenges remain regarding the further application of LOBs, e.g., the poor cyclability induced by cathode passivation and electrolyte decomposition, fast Li depletion and safety concerns due to the corrosion and dendritic growth of Li.[7-10] Considerable efforts have been devoted to the optimization/protection of Li anodes[11-15] and electrolytes,[16-18] aiming to extend the cycle life of LOBs. From the perspective of whole battery operation, the sluggish kinetics of the oxygen reduction reaction (ORR) and oxygen evolution reaction (OER) decreased the formation and decomposition of solid lithium peroxide (Li_2O_2) ($2\,Li^+ + O_2 + 2e^- \leftrightarrow Li_2O_2\,, E_0 =$ 2.96 V), [19] thus leading to many technical issues, i.e., cathode passivation with irreversible damage to the cathode associated with the capacity loss, accumulation of discharge products and by-products (LiOH and/or Li_2CO_3, etc.).[20-22]

To optimize the OER kinetics, various catalysts, including noble metals, [23-26] transition metal oxides, [27-29] nitrides [30-32] and perovskites, [33-34] have been used. However, the severe accumulation of degraded Li_2O_2 at the Li_2O_2/electrode interface readily interrupts the reaction on the electrode. [19,35]

The residue then impedes the catalytic effect, increases the polarization of the battery and hinders the formation and decomposition of Li_2O_2 in the following cycles. It has been noted that small grains and amorphous Li_2O_2 exhibit higher decomposition rates than those of large crystals.[35-36] Some catalysts, such as Co_3O_4 and Pd nanoparticles, are able to increase the decomposition efficiency by forming amorphous Li_2O_2.[37] Nevertheless, some catalytically inactive particles are found to promote battery performance by tuning the Li_2O_2 morphology, e.g., the use of silica as a structural promoter to facilitate nanosized Li_2O_2 formation[38] and NiO as a grain refiner to reduce the average size of Li_2O_2.[39] However, their functions are often lost after a period of battery reaction, which are observed in association with the cladding of discharge products.

Recently, liquid metal (LM)-enabled energy storage technology has attracted much attention due to its unique features, such as softness, deformability, high ductility and self-healing properties.[40-42] Among these liquid metal candidates, gallium (Ga) stands out as a representative material for its low melting temperature of approximately 29 ℃, and indium (In) and/or tin (Sn) are usually introduced to adjust the melting point of Ga to fit the needs of different applications. Ga-based liquid metal-modified carbon has been widely used in Li-ion batteries and Li metal batteries to prevent anodes from cracking and pulverization.[43-45]

Herein, we present a novel LOB cathode strategy based on Ga-Sn liquid metal (LM)-modified multi-walled carbon nanotubes (MWNTs) for alleviating cathode passivation. Benefitting from deformability and self-healing properties, LM can preserve its morphology during long-term cycling; moreover, it helps to reduce the Li_2O_2 size by changing the morphology. Small Li_2O_2 flakes were observed to grow on the mobile surface of conductive LM and also on the MWNTs, which promoted

63 the decomposition of Li_2O_2, subsequently leading to significant enhancements in the rate
64 performance and ultimate capacity and alleviating the depletion of the Li anode; thus, the cyclic
65 stability of LOBs was improved.

66 **EXPERIMENTAL**

67 Gallium (Ga, 99.999%) and tin (Sn, 99.999%) were purchased from Shenyang Jiabei
68 Commercial Trading Company. Multi-walled carbon nanotubes (MWNTs, outer diameter ~ 10 nm, L
69 = 3-6 μm, Sigma-Aldrich), ethanol (>99.7%, AR, Sinopharm), dimethyl ether (DME, anhydrous,
70 99.5%, Sigma-Aldrich), 3-sulfo-N-mercaptopropionamide (95%, Sigma-Aldrich), carbon paper
71 (TORAY, TGP-H-060) and borosilicate glass fibre filter paper (GF, Whatman) were used as received.
72 Prior to use, propylene carbonate (PC, anhydrous, 99.7%, Sigma-Aldrich) and dimethyl sulfoxide
73 (DMSO, anhydrous, 99.9%, Sigma-Aldrich) were dehydrated with activated 4 Å molecular sieves,
74 lithium perchlorate ($LiClO_4$, 99.99%, Sigma-Aldrich) was dried at 160 ℃ in a vacuum oven for 12 h,
75 and Li plates (Shenzhen Poxon Machinery Technology Co. Ltd.) were immersed in 0.1 M $LiClO_4$/PC
76 solution for at least 48 h.

77 **Functionalization of the MWNT cathodes.** The liquid metal (LM) was prepared by melting
78 2.27 g of Sn at 300 °C in a graphite crucible under an Ar atmosphere to alloy with 16.64 g of Ga. A
79 total of 0.9 g of the as-prepared LM was added dropwise to 3.75 mL ethanol with 0.9 mg of
80 3-sulfo-N-mercaptopropionamide, which was dispersed into small drops with probe ultrasonication.
81 The mixture was saturated at room temperature for 3 h, and then the floating phase of the suspension
82 was separated and dried at 80 °C for 10 h. Ten milligrams of the treated LM powder was added to 2
83 mL ethanol, followed by mixing in an ultrasonic bath for 1 h.

The LM-MWNT electrode was fabricated by adding 10 mg of MWNTs to 20 mL ethanol, followed by ultrasonic mixing for 30 minutes. The slurry was sprayed onto carbon paper with a loading of 0.1 mg cm^{-2}. Then, 1 cm^2 square pieces were cut off and dried overnight in a vacuum oven at 60 °C, and a pristine MWNT cathode was prepared. The LM-functionalized MWNT electrodes were prepared using three different methods for comparison: (1) Ga-Sn LM was directly dropped onto carbon paper at a loading of 0.2 mg cm^{-2}, which was coded as LM; (2) MWNTs were pre-mixed with LM suspension during ultrasonic mixing, and then the mixture was sprayed onto carbon paper with a loading of 0.1 mg cm^{-2} MWNTs and 0.2 mg cm^{-2} LM, which was coded as m-LM/MWNT; (3) 0.2 mg of LM suspension was dropped onto MWNTs (0.1 mg cm^{-2}) on carbon paper (1 cm^2) and then dried in a vacuum oven at 60 °C overnight, which was coded as LM/MWNT. An amount of 0.2 mg of LM on the cathode (1 cm^2) is the optimized value, and the details are presented in Fig. S5.

Li-O_2 battery assembly and measurement. The 2032 coin cell was assembled in an argon-filled glovebox (Mikrouna Co. Ltd., H_2O < 0.1 ppm, O_2 < 0.1 ppm), where the Li anode (diameter = 14 mm), separator and cathode were placed in sequence, followed by the addition of 100 μL of 1 M $LiClO_4$/DMSO electrolyte. The cells were measured using a battery testing system (CT-3008W-5V10mA, Neware Technology Co. Ltd., China) in an oxygen atmosphere (≥99.9%, 1.1 atm) with a potential window from 2.0 V to 4.5 V with a capacity of 0.1 mAh at current densities of 0.1, 0.3 and 0.5 mA cm^{-2}.

In situ optical microscopic observation was carried out in a home-made electrochemical cell equipped with a quartz window, in which a copper plate covered by insulating coating was used to conduct current (0.5 mA) to a Ga-Sn LM drop cathode through a hole with a diameter of 0.5 mm,

with a bare Cu electrode as the anode. O_2 saturated 1 M $LiClO_4$ in DMSO was employed as the electrolyte to immerse the both electrodes in the cell. The formation of discharge product on the LM drop was observed and recorded to study the discharge process on the mobile surface of LM.

Characterization. The morphological information of the Ga-Sn LM cathode Li anode was determined using field-emission scanning electron microscopy and energy dispersive spectroscopy (SEM/EDS, S-4800, Hitachi) mapping methods. Structure measurements were carried out using an X-ray diffractometer (XRD, X'Pert PRO) equipped with Cu Kα radiation and a Raman spectrometer (Thermo Fisher Scientific DXR) with a 532-nm laser.

RESULTS AND DISCUSSION

Morphological and structural identification of LM functionalized cathode. Fig. 1a illustrates the procedure for Ga-Sn LM and the three types of cathodes. Sn is introduced to decrease the melting point of Ga, so the melting point of the Ga-Sn alloy (Ga: Sn = 88:12 by weight, 11.8:1 by atom) is approximately 20 °C according to the Ga-Sn phase diagram.[43] At room temperature, the silver grey-coloured Ga-Sn LM presents high surface tension and fluidity (Fig. S1). The XRD spectrum (Fig. 1b) of the Ga-Sn LM (black line) exhibits a broad peak in the range of 29.6° ~ 49.7°, demonstrating a grain production region with short-range order, which is typical of liquid metal, and the diffraction peak at 35.2° assigned to Ga_2O_3 overlaps the broad peak. The chemical stability of the Ga-Sn LM is investigated after soaking it in electrolyte for 4 days, and the XRD spectrum (Fig. 1b, red line) is almost the same as that of the pristine Ga-Sn LM, demonstrating that Ga-Sn LM is stable in an electrolyte attributed to the protection of the Ga_2O_3 film on the surface. The effect of surface oxidation on electric conductance was investigated by measuring the LM with oxide film

encapsulated in a homemade equipment (see Fig. S2), where the conductivity was tested as high as 0.26×10^7 S cm^{-1}, which means that the formation of Ga_2O_3 film does not apparently decreases the electric conductivity of LM, possibly due to its thickness is low.

We used a needle tip to make contact on surface of a LM droplet to study the deformability and recovery property of Ga-Sn LM shown in Fig.S3. Pristine Ga-Sn LM presents as sphere shape on the carbon paper (Fig.S3a, left), once the needle tip was used to contact the sphere surface, the contact tangent plane becomes flattened (Fig.S3a, middle), it recovers immediately after the needle was removed (Fig.S3a, right). Fig.S3b and Fig.S3c show the deformability and recovery property of Ga-Sn LM droplets fully covered by discharge products Li_2O_2 and LiOH, respectively. It can be seen that the deformation of covered Ga-Sn LM droplets has full recovery which is the same to the pure LM droplet. We also dried all droplets at 60 °C overnight, similar deformation and recovery phenomena still exist (Fig.S3d, S3e, S3f). These results indicate that Ga-Sn LM possess deformability and self-healing properties, which may recover from the deformation arisen at the discharging and charging process.

Fig. 1c-1f shows the SEM observation results for the morphologies of all the as-prepared cathodes. Fig. 1c and Fig. 1d display the morphologies of the MWNT and LM cathode, in which the MWNTs and LM (including spheres and particles) are directly dispersed on carbon paper. For the m-LM/MWNT cathode (Fig. 1e), the LM particles are wrapped with MWNTs owing to the pre-mixing process before spraying onto carbon paper. Fig. 1f shows the morphology of the LM/MWNT cathode, where LM particles are dispersed on the MWNTs. EDS analysis of the LM/MWNT cathode is shown in Fig. 1g-k. The SEM image in EDS mode (Fig. 1g) presents bright

147 particles corresponding to signals of Ga and Sn (Fig. 1i and 1j), which overlap, demonstrating that
148 the particles contain Ga and Sn and disperse on the MWNTs (Fig. 1h). The particle size of the Ga-Sn
149 LM ranges from 100 nm to 800 nm with an average of 210 nm (inset of Fig. 1g), and the atomic ratio
150 of Ga:Sn is 13.9:1 (Fig. 1k), which agrees with the ratio of Ga and Sn during preparation.

151 **Electrochemical performance**. The electrochemical performance of the MWNT and LM-based
152 cathodes was assessed using cyclic voltammetry analysis. The assembled batteries with MWNT, LM,
153 m-LM/MWNT, and LM/MWNT cathodes are tested in both Ar and O_2 atmospheres. As shown in Fig.
154 S4, there are no redox peaks in the Ar atmosphere (black lines). In the O_2 atmosphere (red lines),
155 MWNT, LM, m-LM/MWNT, and LM/MWNT cathodes show a peak of oxygen reduction reaction at
156 approximately 2.46, 2.55, 2.39 and 2.46 V with currents of 0.37, 0.05, 0.21 and 0.40 mA,
157 respectively.

158 The cells were analyzed using galvanostatic charge/discharge tests at a capacity of 0.1 mAh and
159 current density of 0.1 mA cm^{-2}, and the performance of all the cells is displayed in Fig. 2. With
160 MWNTs as the cathode (Fig. 2a), the cell's charge potential (at 0.05 mAh) reaches 3.91 V with an
161 overpotential gap of 1.28 V in the first cycle, which increases to 4.04 V (with an overpotential gap of
162 1.42 V) at the 20^{th} cycle and 4.2 V (with an overpotential gap of 1.51 V) at the 40^{th} cycle, but the
163 battery can only cycle for 50 times. The charge-discharge curves of the LM cell are shown in Fig. 2b.
164 In the first cycle, the charge potential of LM is 3.94 V with an overpotential gap of 1.21 V, which is
165 slightly lower than that of the MWNT cathode. Then, the charge potential increases to 4.05 V at the
166 20^{th} cycle with an overpotential of 1.31 V and further increases slowly up to the 98^{th} cycle. With the
167 m-LM/MWNT cathode (Fig. 2c), the charge potential of the first cycle is 3.65 V with a potential gap

of 0.93 V, much lower than those of the MWNT and LM cathodes. Next, the charge potential increases to 3.84 V (with an overpotential gap of 1.08 V) at the 5^{th} cycle and to 4.02 V (with an overpotential gap of 1.25 V) at the 20^{th} cycle and then increases slowly to 4.10 V (with an overpotential gap of 1.38 V) at the 70^{th} cycle. The battery with the m-LM/MWNT cathode can run for 119 cycles, which is much longer than the MWNT cathode. The cell with the LM/MWNT cathode presents a charge potential of 3.44 V at 0.05 mAh and an overpotential gap of 0.71 V, which are much lower than those of the other three cells. The charge potential of the LM/MWNT cathode is 3.73 V (with an overpotential of 0.99 V) at the 5^{th} cycle, 3.95 V (with an overpotential of 1.2 V) at the 20^{th} cycle, and 4.15 V (with an overpotential of 1.45 V) at 120 cycles. The battery with LM/MWNT demonstrates the best performance of all tested cells, presenting the lowest overpotential of the cathodes at the same cycle number and the lowest degradation at 200 cycles.

Fig. 2e-h shows the specific capacity, discharge and charge terminal potential as a function of the cycling process. The discharge terminal potentials (at 0.1 mAh) are maintained at approximately 2.7 V for all four cells until failure; the main difference among these four cathodes is the charge terminal potential (at 0.1 mAh). For the MWNT (Fig. 2e), the terminal potential begins at 4.0 V, then increases quickly to 4.3 V at the 20^{th} cycle and 4.5 V at the 40^{th} cycle. The charge terminal potential of the LM cathode is initially slightly higher than 4.0 V, increases slower than the MWNT and reaches 4.5 V at the 90^{th} cycle (Fig. 2f). For the m-LM/MWNT cathode (Fig. 2g), the initial terminal potential is approximately 3.8 V, then increases to 4.0 V at the 10^{th} cycle, 4.2 V at the 94^{th} cycle and 4.5 V at the 119^{th} cycle. The charge terminal potential of the LM/MWNT cathode is initially approximately 3.5 V, increases to 4.0 V at the 20^{th} cycle and then slowly reaches 4.2 V at the 105^{th} cycle and 4.5 V at the 200^{th} cycle (Fig. 2h). Generally, the kinetics process of the Li electrode is

rather simple; thus, the charge overpotential originates primarily from the oxidation of Li_2O_2 at the cathode.[46-48] Therefore, the Li_2O_2 formed at the LM/MWNT cathode tends to decompose more than those formed on other cathodes according to the lower charge overpotential.

The rate performance of the cells at high charge-discharge current density was studied. At 0.1 mA cm^{-2} (Fig. 2i), the cells with MWNT, LM, m-LM/MWNT, and LM/MWNT cathodes can run 50, 98, 119 and 200 times, respectively. The cycle numbers trend downward to 30, 44, 86, and 138 cycles at 0.3 mA cm^{-2} (Fig. 2j) and further drop to 25, 22, 50, and 102 cycles at 0.5 mA cm^{-2} (Fig. 2k). The full-discharge capacities (discharge to 2.0 V) of the MWNT, LM, m-LM/MWNT, and LM/MWNT cathodes are shown in Fig. 2l. For the MWNT and LM cathodes, the discharge curves show a short discharge plateau followed by a sharp decrease, and the discharge times are 2.9 h and 1.9 h, with full-discharge capacities of 0.29 mAh (2900 mAh g_{MNWTs}^{-1}) and 0.19 mAh (950 mAh g_{LM}^{-1}), respectively. For the m-LM/MWNT and LM/MWNT cathodes, the discharge time is dramatically increased with a long discharge plateau. The discharge time of the m-LM/MWNT cathode is 17.3 h, with a full-discharge capacity of 1.73 mAh (5760 mAh $g_{MNWTs+LM}^{-1}$). The LM/MWNT cathode displays a discharge time of 21.4 h and a full-discharge capacity of 2.14 mAh (7133 mAh $g_{MNWTs+LM}^{-1}$). To understand how this discharge capacity is generated, we discharge the cell with the LM/MWNT cathode in an Ar atmosphere, of which the discharge potential decreases sharply without a plateau, displaying a discharge time of 0.45 h. The results suggest that the LM/MWNT cathode has the lowest overpotential, largest full-discharge capacity, and longest cycle life, and the presence of both MWNTs and LM at the reaction interface is essential for enhancing the battery performance, where the distribution of the LM on the MWNTs yields better performance than the wrapping of the LM with MWNTs.

Cathode and anode appearance after battery discharge. The morphology and structure of the discharged products on the cathodes are characterized and are shown in Fig. 3. Precipitation of sheet-like and flower-like products can be observed on the MWNT cathode (Fig. 3a). On the LM cathode (Fig. 3b), the discharge products coated on the LM particles result in a rough surface. On the m-LM/MWNT cathode (Fig. 3c), similar to the MWNT cathode, sheet-like and flower-like products (insertion images) are observed on both the LM particles and MWNTs, which is due to the MWNTs wrapping over the LM, leading to surface properties similar to those of the pure MWNTs. The morphology of the discharge products on the LM/MWNT cathode is different from those on the MWNT, LM and m-LM/MWNT cathodes, where flakes with an average length of 105 nm and an average width of 55 nm are vertically attached to the large particles as well as to the MWNTs, as shown in the high-resolution image (insert). The Ga, Sn and O elemental maps (Fig. 3e) of the red frame in Fig. 3d demonstrate that the large particles are Ga-Sn LM and the O originating from the discharge products overlap with both the LM and MWNTs, which further demonstrates the discharge products growing on the LM and MWNTs.

TEM image of pristine Ga-Sn LM presents a smooth surface (Fig. S6a), Li_2O_2 flakes can be observed after discharge process (Fig. S6b). HRTEM image displays that the surface deposit contains Ga_2O_3 (inset of Fig.S6c, region 1) with the lattice spacing of 0.29 nm corresponding to (-401) facet and Li_2O_2 (inset of Fig.S6c, region 2) with the interplanar spacing of 0.27 nm corresponding to (200) facet, and no Li_2O_2 crystal appears to grow on the Ga_2O_3 seed. The *in situ* optical observation further shows that the discharge products flow along the surface of Ga-Sn LM during discharge process when they become lager. This suggests that the mobility and high surface tension make the discharge products flow away and always leave LM surface available for the ORR and OER processes.

234 It is also noticed that the incorporation of LM changes the morphology of discharge products in
235 the Li-O_2 cells. On the MWNTs surface, the discharge product appears as large Li_2O_2 crystals (the
236 inset of Fig. 3a), and on the m-LM/MWNTs cathode flower-like crystals are also formed for the LM
237 drops wrapped by MWNTs. On the LM/MWNTs cathode, small flaky Li_2O_2 are seen on LM drops
238 and MWNTs. The ring current of RRDE polarization curves (Fig. S7, blue dot line) of the MWNT
239 cathode indicates that the LiO_2 is generated in ORR process, which diffuses into electrolyte and
240 forms large Li_2O_2 crystals. For the LM/MWNT, the ring current of RRDE polarization curves (Fig.
241 S7, red dot line) is higher than the one of MWNT, suggesting that more LiO_2 is produced in the
242 electrolyte, lead to small flaky Li_2O_2 since more Li_2O_2 nuclei are available.

243 The structure of the discharge products was characterized by Raman spectroscopy, as shown in
244 Fig. S8. For both the MWNT and LM/MWNT cathodes, the peaks at approximately 784 cm^{-1} are
245 attributed to Li_2O_2,[19] indicative of Li_2O_2 as a discharge product, and the peaks at 202 cm^{-1} , 252 cm^{-1}
246 and 336 cm^{-1} (red line) observed for the LM/MWNT cathode are attributed to Ga-Sn LM.[47,48] XRD is
247 also used to characterize the structure of the discharge products. As shown in Fig. 3f, the discharge
248 products formed on the MWNT and LM/MWNT present five peaks at 32.9°, 35.0°, 40.6°, 47.4° and
249 49.0°, corresponding to the (100), (101), (102), (004) and (103) facets of Li_2O_2, respectively. The
250 chemical stability of the discharge products was also tested. The XRD spectrum of the LM/MWNT
251 soaked in electrolyte for 4 days shows that the structure of the discharge products does not change,
252 indicating that the discharge products are relatively stable in the electrolyte. These results
253 demonstrate that the morphology and size of Li_2O_2 are influenced by the cathode structure, while the
254 components of the discharge products remain unchanged. The LM/MWNT cathode promotes the
255 formation of small-sized Li_2O_2, which may be the reason for the high battery performance.

To investigate the LM influence on cathode passivation, the morphology evolution on the cathode surface of the LM/MWNT, as the optimum structure, was compared with that of the bare MWNT cathode. After 50 cycles, the MWNT cathode was completely covered with the discharge products (Fig. 3g), which indicates that the cathode passivation is severe. In contrast, after 50 cycles of the LM/MWNT cell, the bare MWNT is still visible together with the flaky discharge products (Fig. 3h). From SEM and EDS elemental mapping analyses (Fig. S9), it can be observed that the surface of the LM particles is smooth, which demonstrates that the discharge products on the LM are decomposed completely. Even after 200 cycles, as shown in Fig. 3i and Fig. S10, a smooth LM can still be observed on the LM/MWNT cathode, available for Li_2O_2 formation. The Ga-Sn LM morphology does not change during the discharge/charge cycling process, benefiting from the deformability and self-healing properties of LM. The evolution of the cathode demonstrates that the passivation on LM/MWNT is alleviated, which facilitates Li_2O_2 decomposition, especially along the Ga-Sn LM surface. The final products on the MWNT and LM/MWNT cathodes after cell failure were characterized by XRD. As shown in Fig. S11, both cathodes present peaks at 26.6°, 54.8°attributing to MWNT, and peak at 32.5 corresponding to LiOH, respectively.

Li anode corrosion may take place due to the decomposition of the electrolyte, which is caused by inhibited cathode passivation and suppressed charge/discharge polarization. The pristine Li anode shows a smooth surface with a thickness of 323 μm (Fig. 4a), and it completely crumbles to powder after only 50 cycles in the cell with the MWNT cathode (Fig. 4b). Nevertheless, in the cell with LM/MWNT as the cathode, the Li anode exhibits a relatively flat surface with a thickness of approximately 173 μm after 50 cycles (Fig. 4c), and the crumbling occurs after 200 cycles (Fig. 4d). The powders on the Li anodes were collected and characterized as LiOH by XRD in both cells with

MWNT and LM/MWNT cathode (Fig. S12). The above results proved that the corrosion of the Li anode was alleviated by using Ga-Sn LM, possibly by reduced polarization.

CONCLUSIONS

We described a new high-performance Li-O_2 cathode with Ga-Sn LM functionalized MWNTs. The results indicated that the incorporation of LM and MWNT (LM/MWNT) on the reaction interface is essential to achieve optimized battery performance. The LM/MWNT increases the full-discharge capacity to 2.14 mAh, which is nearly 7.4 times higher than that of the bare MWNT cathode. The LM/MWNT also promotes the decomposition of discharge products by inducing the formation of flaky Li_2O_2 that is smaller than the sheet/flower crystals formed on pristine MWNTs. Moreover, the corrosion of the Li anode is alleviated with the presence of Ga-Sn LM on the cathode. Thus, the LM/MWNT cathode can extend the cycle life to 200 cycles, which is much longer than that of MWNT (50 cycles). However, the morphological evolution of Li_2O_2 with the LM/MWNT cathode is not yet understood, and we will study this mechanism in the future. We hope this research inspires new ideas for cathode protection for the practical application of Li-O_2 batteries.

ASSOCIATED CONTENT

Supporting Information.

The Supporting Information is available free of charge at https://

Photo of Ga-Sn LM, CV curves of LOBs, cyclic performance of LOBs, Raman spectra of LOBs cathodes after discharge, SEM images, XRD patterns, Video

AUTHOR INFORMATION

Corresponding Authors

Kun Luo - *School of Materials Science and Engineering, Changzhou University, Changzhou 213164, P. R. China; Email: luokun@cczu.edu.cn.*

Terence Xiaoteng Liu - *Department of Mechanical & Construction Engineering, Faculty of Engineering and Environment, Northumbria University, Newcastle upon Tyne, NE1 8ST, UK; Email: terence.liu@northumbria.ac.uk.*

Present Addresses

Zhihong Luo - *College of Materials Science and Engineering, Guilin University of Technology, Guilin 541004, P. R. China*

Chenhao Ji - *College of Materials Science and Engineering, Guilin University of Technology, Guilin 541004, P. R. China*

Liankun Yin - *College of Materials Science and Engineering, Guilin University of Technology, Guilin 541004, P. R. China*

Guangbin Zhu - *College of Materials Science and Engineering, Guilin University of Technology, Guilin 541004, P. R. China*

Ben Bin Xu - *Department of Mechanical & Construction Engineering, Faculty of Engineering and Environment, Northumbria University, Newcastle upon Tyne, NE1 8ST, UK*

Yucheng Wang - *Department of Mechanical & Construction Engineering, Faculty of Engineering and Environment, Northumbria University, Newcastle upon Tyne, NE1 8ST, UK*

Xiangqun Zhuge - *School of Materials Science and Engineering, Changzhou University, Changzhou 213164, P. R. China*

Complete contact information is available at: https://

Author Contributions

The manuscript was written through contributions of all authors. All authors have given approval to the final version of the manuscript.

Notes

The authors declare no conflict of interest.

ACKNOWLEDGMENT

This work was supported by the National Natural Science Foundation of China (Grant No. 51874051), the UK Engineering Physics and Science Research Council (Grant No. EP/S032886/1), Natural Science Foundation of Guangxi (Grant No. 2018GXNSFAA281184 and 2019GXNSFAA245046), Guangxi Innovation Driven Development Project（Grant No. AA17204021) and the foundation of Guangxi Key Laboratory of Optical and Electronic Materials and Devices.

REFERENCES

[1] Z. Ma, X. Yuan, L. Li, Z. Ma, D. Wilkinson, L. Zhang, J. Zhang, A review of cathode materials and structures for rechargeable lithium-air batteries, Energy. Environ. Sci. 8 (2015) 2144-2198.

[2] P. Zhang, Y. Zhao, X. Zhang, Functional and stability orientation synthesis of materials and

337 structures in aprotic Li-O_2 batteries, Chem. Soc. Rev. 47 (2018) 2921-3004.

338 [3] Y. Liu, L. Yue, P. Lou, G. Xu, J. Liang, P. Guo, J. Wang, R. Tao, Y. Cao, L. Shi, Liquid metal
339 modified $Li_4Ti_5O_{12}$ with improved conductivity as novel anode material for lithium-ion batteries,
340 Mater. Lett. 58 (2020) 126803.

341 [4] P. Wang, Z. Chen, H. Wang, Z. Ji, Y. Feng, J. Wang, J. Liu, M. Hu, J. Fei, W. Gan, Y. Huang, A
342 high-performance flexible aqueous Al ion rechargeable battery with long cycle life, Energy. Storage.
343 Mater. 25 (2020) 426-435.

344 [5] Y. Huang, Z. Li, Z. Pei, Z. Liu, H. Li, M. Zhu, J. Fan, Q. Dai, M. Zhang, L. Dai, C. Zhi,
345 Solid-state rechargeable Zn//NiCo and Zn-air batteries with ultralong lifetime and high capacity: the
346 role of a sodiumpolyacrylate hydrogel electrolyte, Adv. Energy. Mater. 8 (2018) 11.

347 [6] M. Chen, J. Xiao, W. Hua, Z. Hu, W. Wang, Q. Gu, Y. Tang, S. Chou, H. Liu, S. Dou, A cation
348 and anion dual doping strategy for the elevation of titanium redox potential for high-power
349 sodium-ion batteries, Angew. Chem. Int. Ed. 59 (2020) 12076-12083.

350 [7] F. Li, T. Zhang, H. Zhou, Challenges of non-aqueous Li-O_2 batteries: electrolytes, catalysts, and
351 anodes, Energy. Environ. Sci. 61 (2013) 125-1141.

352 [8] Y. Shao, F. Ding, J. Xiao, J. Zhang, W. Xu, S. Park, J. Zhang, Y. Wang, J. Liu, Making Li-air
353 batteries rechargeable: material challenges, Adv. Funct. Mater. 23 (2013) 987-1004.

354 [9] L. Grande, E. Paillard, J. Hassoun, J. Park, Y. Lee, Y. Sun, S. Passerini, B. Scrosati, The
355 lithium/air battery: still an emerging system or a practical reality? Adv. Mater. 27 (2015) 784-800.

356 [10] S. Ma, Y. Zhang, Q. Cui, J. Zhao, Z. Peng, Understanding oxygen reactions in aprotic Li-O_2
357 batteries, Chin. Phys. B. 25 (2016) 58-67.

358 [11] B. Kim, J. Kim, J. Min, Y. Lee, J. Choi, M. Jang, S. Freunberger, J. Choi, A moisture-and

oxygen-impermeable separator for aprotic Li-O_2 batteries, Adv. Funct. Mater. 26 (2016) 1747-1756.

[12] K. Luo, G. Zhu, Y. Zhao, Z. Luo, X. Liu, K. Zhang, Y. Li, K. Scott, Enhanced cycling stability of Li-O_2 batteries by using a polyurethane/SiO_2/glassfiber nanocomposite separator, J. Mater. Chem. A 6 (2018) 7770-7776.

[13] Z. Luo, G. Zhu, L. Guo, F. Li, Y. Li, M. Fu, Y. Cao, Y. Li, K. Luo, Improving the cyclability and capacity of Li-O_2 batteries via low rate pre-activation, Chem. Commun. 55 (2019) 2094-2097.

[14] Z. Sun, H. Wang, J. Wang, T. Zhang, Oxygen-free cell formation process obtaining LiF protected electrodes for improved stability in lithium-oxygen batteries, Energy Storage Mater. 23 (2019) 670-677.

[15] T. Liu, Y. Yu, X. Yang, J. Wang, X. Zhang, Lithium and stannum hybrid anodes for flexible wire type lithium oxygen batteries, Small Structures. 4 (2020).

[16] R. Liu, Y. Lei, W. Yu, H. Wang, L. Qin, D. Han, W. Yang, D. Zhou, Y. He, D. Zhai, B. Li, F. Kang, Achieving low overpotential lithium-oxygen batteries by exploiting a new electrolyte based on N,N'-Dimethylpropyleneurea, ACS. Energy. Lett. 2 (2017) 313-318.

[17] B. Liu, W. Xu, P. Yan, S. Kim, M. Engelhard, X. Sun, D. Mei, J. Cho, C. Wang, J. Zhang, Stabilization of Li metal anode in DMSO-based electrolytes via optimization of salt-solvent coordination for Li-O_2 batteries, Adv. Energy. Mater. 7 (2017) 10.

[18] J. Zhao, H. Lu, X. Zhao, O. Malyi, J. Peng, C. Lu, X. Li, Y. Zhang, Z. Zeng, G. Xing, Y. Tang, Printable ink design towards customizable miniaturized energy storage devices, ACS Materials Lett. 2 (2020) 1041-1056.

[19] J. Wang, Y. Zhang, L. Guo, E. Wang, Z. Peng, Identifying reactive sites and transport limitations of oxygen reactions in aprotic lithium-O_2 batteries at the stage of sudden death, Angew.

Chem. Int. Ed. 55 (2016) 5201-5205.

[20] H. Yuan , J. Read, Y. Wang, Capacity loss of non-aqueous Li-Air battery due to insoluble product formation: Approximate solution and experimental validation, Mater Today Energy. 14 (2019) 100360.

[21] R. Black, S. Oh, J. Lee, T. Yim, B. Adams, L. Nazar, Screening for superoxide reactivity in Li-O_2 batteries: effect on Li_2O_2/LiOH crystallization, J. Am. Chem. Soc. 134 (2012) 2902-2905.

[22] T. Zhang, H. Matsuda, H. Zhou, Gel-derived cation-π stacking films of carbon nanotube-graphene complexes as oxygen cathodes, ChemSusChem. 7 (2014) 2845-2852.

[23] J. Lu, Y. Lei, K. Lau, X. Luo, P. Du, J. Wen, R. Assary, U. Das, D. Miller, J. Elam, H. Albishri, D. AbdEl-Hady, Y. Sun, L. Curtiss, K. Amine, A nanostructured cathode architecture for low charge overpotential in lithium-oxygen batteries, Nat. Commun. 4 (2013) 2383.

[24] K. Song, J. Jung, M. Park, H. Park, H. Kim, S. Choi, J. Yang, K. Kang, Y. Han, Y. Kang, Anisotropic surface modulation of Pt catalysts for highly reversible Li-O_2 batteries: high index facet as a critical descriptor, ACS. Catal. 8 (2018) 9006-9015.

[25] J. Xu, Z. Chang, Y. Wang, D. Liu, Y. Zhang, X. Zhang, Cathode surface-induced, solvation-mediated, micrometer-sized Li_2O_2 cycling for Li-O_2 batteries, Adv. Mater. 28 (2016) 9620-9628.

[26] B. Sun, L. Guo, Y. Ju, P. Munroe, E. Wang, Z. Peng, G. Wang, Unraveling the catalytic activities of ruthenium nanocrystals in high performance aprotic Li-O_2 batteries, Nano. Energy. 28 (2016) 486-494.

[27] Y Cao, M. Zheng, S. Cai, X. Lin, C. Yang, W. Hu, Q. Dong, Carbon embedded α-MnO_2@graphene nanosheet composite: A bifunctional catalyst for high performance lithium

403 oxygen batteries, J. Mater. Chem. A 2 (2014) 18736-18741.

404 [28] Y. Zhou, Z. Lyu, L. Wang, W. Dong, W. Dai, X. Cui, Z. Hao, M. Lai, C. Wei, Co_3O_4
405 functionalized porous carbon nanotube oxygen-cathode to promote Li_2O_2 surface growth for
406 improved cycling stability in Li-O_2 batteries, J. Mater. Chem. A 5 (2017) 25501-25508.

407 [29] J. Wang, R. Zhan, Y. Fu, H. Yu, C. Jiang, T. Zhang, C. Zhang, J. Yao, J. Li, X. Li, J. Tian,
408 R.Yang, Design and synthesis of hierarchical, freestanding bowl-like NiCo2O4 as cathode for
409 long-life Li-O2 batteries, Mater Today Energy. 5 (2017) 214-221.

410 [30] Z. Yang, X. Yang, T. Liu, Z. Chang, Y. Yin, X. Zhang, J. Yan, Q. Jiang, In situ CVD derived
411 Co-N-C composite as highly efficient cathode for flexible Li-O_2 batteries, Small. 14 (2018) 1800590.

412 [31] K. Zhang, L. Zhang, X. Chen, X. He, X. Wang, S. Dong, P. Han, C. Zhang, S. Wang, L. Gu, G.
413 Cui, Mesoporous cobalt molybdenum nitride: a highly active bifunctional electrocatalyst and its
414 application in lithium-O_2 batteries, J. Phys. Chem. C 117 (2013) 858-865.

415 [32] J. Liang, Y. Wang, C. Wang, S. Lu, In situ formation of NiO on Ni foam prepared with a novel
416 leaven dough method as an outstanding electrocatalyst for oxygen evolution reactions, J. Mater.
417 Chem. A 4 (2016) 9797-9806.

418 [33] J. Wang, X. Cheng, Z. Li, M. Xu, Y. Lu, S. Liu, Y. Zhang, Perovskite $Sr_{0.9}Y_{0.1}CoO_{3-\delta}$ nanorods
419 modified with CoO nanoparticles as a bifunctional ctalyst for rechargeable Li-O_2 batteries, ACS.
420 Appl. Energy Mater. 1 (2018) 5557-5566.

421 [34] J. Kim, Y. Kim, Y. Noh, S. Lee, Y. Kim, W. Kim, Bifunctional hybrid catalysts with perovskite
422 $LaCo_{0.8}Fe_{0.2}O_3$ nanowires and reduced graphene oxide sheets for an efficient Li-O_2 battery cathode,
423 ACS Appl. Mater. Interfaces. 10 (2018) 5429-5439.

424 [35] L. Song, L. Zou, X. Wang, N. Luo, J. Xu, J. Yu, Realizing formation and decomposition of

425 Li_2O_2 on its own surface with a highly dispersed catalyst for high round-trip efficiency Li-O_2
426 batteries, iscience. 14 (2019) 34-36.
427 [36] B. Gallant, D. Kwabi, R. Mitchell, J. Zhou, C. Thompson, Y. Shao-Horn, Influence of Li_2O_2
428 morphology on oxygen reduction and evolution kinetics in Li-O_2 batteries, Energy. Environ. Sci. 6
429 (2013) 2518-2528.
430 [37] Y. Zhang, Q. Cui, X. Zhang, W. McKee, Y. Xu, S. Ling, H. Li, G. Zhong, Z. Peng, Amorphous
431 Li_2O_2: chemical synthesisand electrochemical properties, Angew. Chem. Int. Ed. 55 (2016)
432 10717-10721.
433 [38] C. Xia, M. Waletzko, K. Peppler, J. Janek, Silica nanoparticles as structural promoters for
434 oxygen cathodes of lithium-oxygen batteries, J. Phys. Chem. C 117 (2013) 19897-19904.
435 [39] S. Ganapathy, Z. Li, M. Anastasaki, S. Basak, X. Miao, K. Goubitz, H. Zandbergen, F. Mulder,
436 M. Wagemaker, Use of nano seed crystals to control peroxide morphology in a nonaqueous Li-O_2
437 battery, J. Phys. Chem. C 120 (2016) 18421-18427.
438 [40] D. Bradwell, H. Kim, A. Sirk, D. Sadoway, Magnesium-antimony liquid metal battery for
439 stationary energy storage, J. Am. Chem. Soc. 134 (2012) 1895-1897.
440 [41] L. Wang, S. Welborn, H. Kumar, M. Li, Z. Wang, V. Shenoy, E. Detsi, High-rate and long
441 cycle-life alloy-type magnesium-ion battery anode enabled through (De) magnesiation-induced
442 near-room-temperature solid-liquid phase transformation, Adv. Energy Mater. 9 **(**2019) 1902086.
443 [42] Y. Ding, X. Guo, Y. Qian, L. Xue, A. Dolocan, G. Yu, Room-temperature all-liquid-metal
444 batteries based on fusible alloys with regulated interfacial chemistry and wetting, Adv. Mater. 32
445 (2020) 2002577.
446 [43] Y. Wu, L. Huang, X. Huang, X. Guo, D. Liu, D. Zheng, X. Zhang, R. Ren, D. Qu, J. Chen, A

447 room-temperature liquid metal-based self-healing anode for lithium-ion batteries with an ultra-long
448 cycle life, Energy. Environ. Sci. 10 (2017) 1854-1861.
449 [44] X. Guo, Y. Ding, L. Xue, L. Zhang, C. Zhang, J. Goodenough, G. Yu, A self-healing
450 room-temperature liquid-metal anode for alkali-ion batteries, Adv. Funct. Mater. 28 (2018) 1804649.
451 [45] G. Zhang, H. Deng, R. Tao, B. Xiao, T. Hou, S. Yue, N. Shida, Q. Cheng, W. Zhang, J. Liang,
452 Constructing a liquid-metal based self-healing artificial solid electrolyte interface layer for Li metal
453 anode protection in lithium metal battery, Mater. Lett. 262 (2020) 127194.
454 [46] C. Shu, J. Wang, J. Long, H. Liu, S. Dou, Understanding the reaction chemistry during
455 charging in aprotic lithium-oxygen batteries: existing problems and solutions, Adv. Mater. 31 (2019)
456 1804587.
457 [47] Y. Choi, W. Kim, Y. Park, S. Lee, D. Bae, Y. Lee, G. Park, W. Choi, N. Lee, J. Kim, Catalytic
458 growth of b-Ga_2O_3 nanowires by arc discharge, Adv. Mater. 12 (2000) 746-750.
459 [48] X. Du, Z. Li, C. Luan, W. Wang, M. Wang, X. Feng, H. Xiao, J. Ma, Preparation and
460 characterization of Sn-doped β-Ga_2O_3 homoepitaxial film by MOCVD, J. Mater. Sci. 50 (2015)
461 3252-3257.

462 **Figure captions**

463 **Figure 1** Illustration of the preparation of Ga-Sn LM and cathodes (a); XRD spectra of Ga-Sn LM
464 (b); SEM images: pristine MWNT (c), LM (d), m-LM/MWNT (e) and LM/MWNT (f); EDS analysis:
465 SEM image of LM/MWNT (inset: size distribution of Ga-Sn LM) (g), elemental mapping of image
466 in red frame: C map (h), Ga map (i), and Sn map (j), and elemental analysis (k).

467 **Figure 2** (a-d) Charge-discharge curves of Li-O_2 batteries: MWNT (a), LM (b), m-LM/MWNT (c)

and LM/MWNT cathodes (d); (e-h) the specific capacities along with the discharge and charge terminal voltages against the cycle number: MWNT (e), LM (f), m-LM/MWNT (g), LM/MWNT (h); (i-k) rate performance of Li-O_2 batteries at 0.1 mA cm^{-2} (i), 0.3 mA cm^{-2} (j) and 0.5 mA cm^{-2} (k); (l) full discharge plots of Li-O_2 batteries with MWNT, LM, m-LM/MWNT, and LM/MWNT cathodes in the O_2 atmosphere and the LM/MWNT cathode in the Ar atmosphere.

Figure 3 SEM images of MWNT (a), LM (b), m-LM/MWNT (c), and LM/MWNT (d) cathodes after discharge, insets: high magnification images corresponding yellow frames; (e) Ga, Sn and O elemental maps corresponding to image in red frame; (f) XRD spectra of discharge products; SEM images of MWNT (g) and LM/MWNT (h) cathodes after 50 cycles, LM/MWNT cathode after 200 cycles (i).

Figure 4 SEM images of pristine Li (a) after 50 cycles (b), Li anode in the cell with LM/MWNT cathode after 50 (c) and 200 cycles (d), inset: the thickness of the corresponding Li anode.

Figure 1

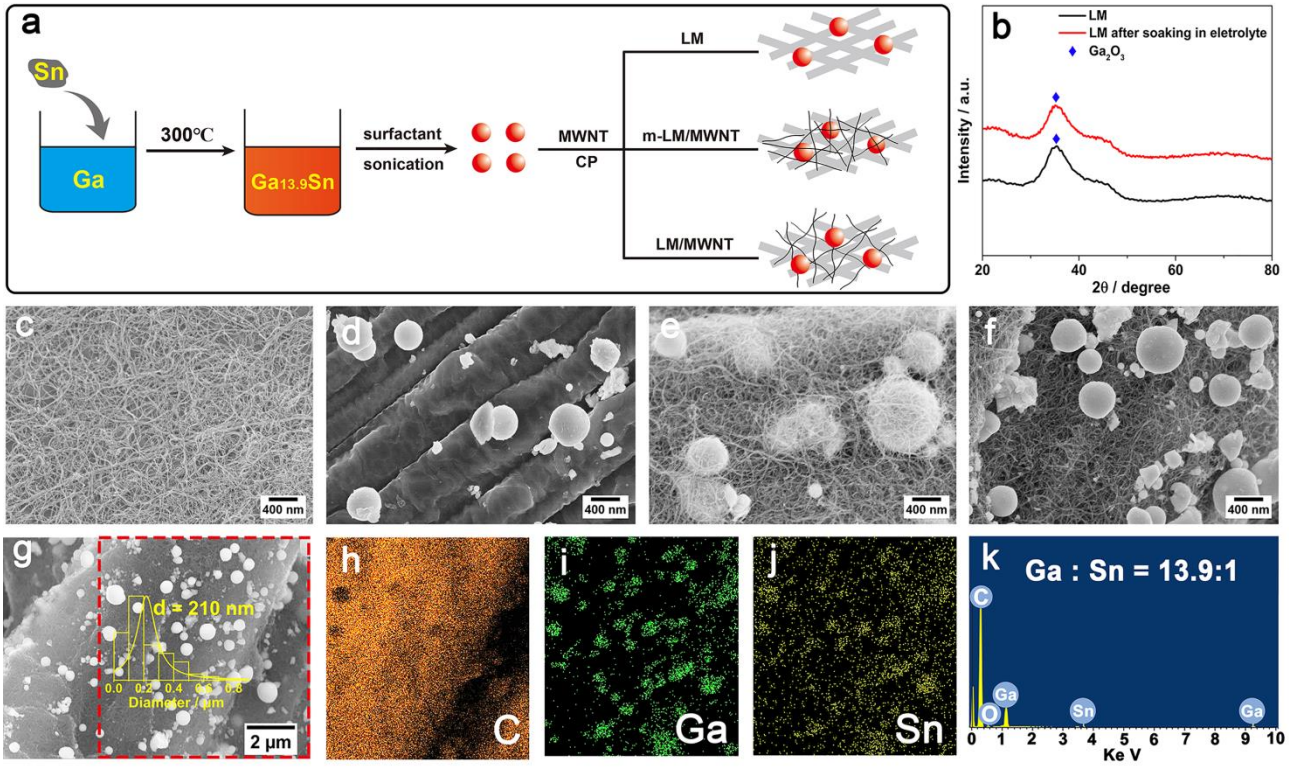

Figure 2

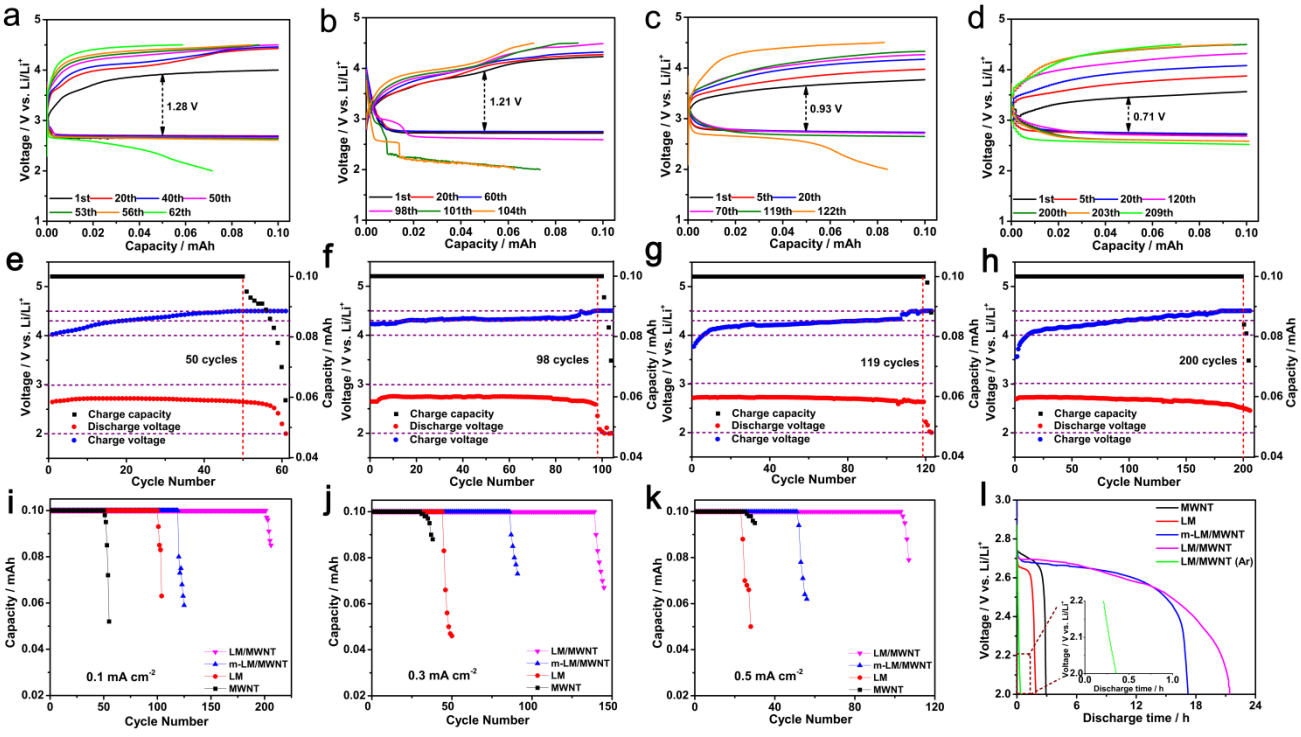

Figure 3

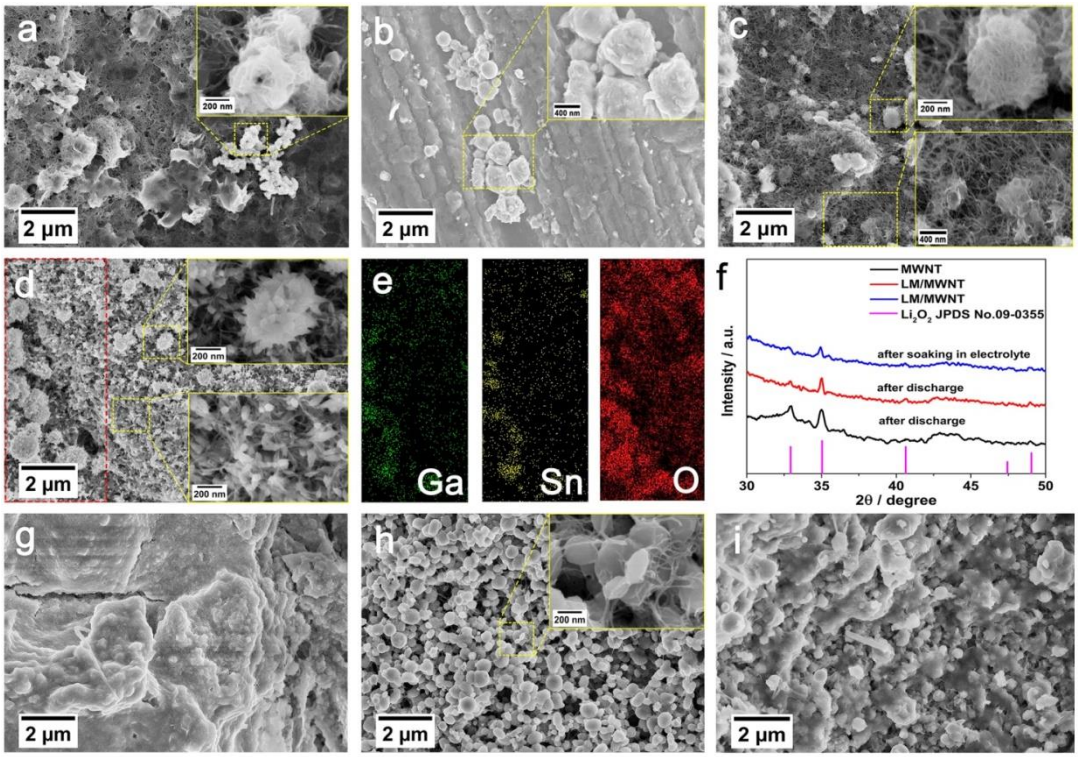

Figure 4